The Astronomical Journal, 165:243 (12pp), 2023 June https://doi.org/10.3847/1538-3881/accf85

High-resolution Observations of H I in the IC 63 Reflection Nebula

Lars Bonne[1], B-G Andersson[1], Robert Minchin[1,2], Archana Soam[1,3], Joshua Yaldaei[4], Kristin Kulas[4], Janik Karoly[1,5], Lewis B. G. Knee[6], Siddharth Kumar[7], and Nirupam Roy[7]
[1] SOFIA Science Center/USRA, NASA Ames Research Center, M.S. N232-12, Moffett Field, CA 94035, USA; lbonne@usra.edu, bg@sofia.usra.edu
[2] National Radio Astronomy Observatory, P.O. Box O, Socorro, NM 87801, USA
[3] Indian Institute of Astrophysics, II Block, Koramangala, Bengaluru 560034, India
[4] Department of Physics, Santa Clara University, Santa Clara, 500 El Camino Real, Santa Clara, CA, USA
[5] Jeremiah Horrocks Institute, University of Central Lancashire, Preston PR1 2HE, UK
[6] Herzberg Astronomy and Astrophysics Research Centre, National Research Council of Canada, 5071 West Saanich Road, Victoria, BC, V9E 2E7, Canada
[7] Department of Physics, Indian Institute of Science, Bangalore 560012, India
Received 2023 January 24; revised 2023 April 19; accepted 2023 April 20; published 2023 May 22

Abstract

Photodissociation regions (PDRs), where the (far-)ultraviolet light from hot young stars interact with the gas in surrounding molecular clouds, provide laboratories for understanding the nature and role of feedback by star formation on the interstellar medium. While the general nature of PDRs is well understood—at least under simplified conditions—the detailed dynamics and chemistry of these regions, including gas clumping, evolution over time, etc., can be very complex. We present interferometric observations of the 21 cm atomic hydrogen line, combined with [C II] 158 μm observations, toward the nearby reflection nebula IC 63. We find a clumpy H I structure in the PDR, and a ring morphology for the H I emission at the tip of IC 63. We further unveil kinematic substructure, of the order of 1 km s^{-1}, in the PDR layers and several legs that will disperse IC 63 in <0.5 Myr. We find that the dynamics in the PDR explain the observed clumpy H I distribution and lack of a well-defined H I/H_2 transition front. However, it is currently not possible to conclude whether H I self-absorption and nonequilibrium chemistry also contribute to this clumpy morphology and missing H I/H_2 transition front.

Unified Astronomy Thesaurus concepts: Photodissociation regions (1223); Interstellar medium (847); Interstellar clouds (834)

1. Introduction

The formation of high-mass (OB) stars leads to stellar feedback in the form of radiation, stellar winds, and eventually supernovae. These feedback processes ionize the surrounding interstellar medium (ISM) and can have an important impact on its dynamical and chemical evolution. At the interface of the fully ionized phase with the molecular phase this creates photodissociation regions (PDRs) where FUV photons with energies between 6 and 13.6 eV dominate the chemistry (Hollenbach & Tielens 1999; Röllig et al. 2007; Wolfire et al. 2022). This leads to a chemical evolution as a function of depth into the cloud due to the decreasing amount of FUV photons. This chemical evolution includes, among (many) others, the transition from atomic to molecular hydrogen (H_2) and from ionized carbon (C^+) to carbon monoxide (CO; e.g., Sternberg & Dalgarno 1995). These different tracers can then also provide a view on the dynamics of the cloud as a function of depth in the PDR which helps to constrain the effect of stellar feedback on molecular cloud evolution (e.g., Schneider et al. 2020). In addition, probing a variety of tracers allows to investigate the physical, dynamic, and chemical structure of the PDR. Often, PDR models are based on plane-parallel geometries (e.g., Tielens & Hollenbach 1985; Kaufman et al. 1999; Le Petit et al. 2006), yet PDR structure can be more complicated in the 3D turbulent ISM. Therefore, dedicated clumpy PDR models have been developed (e.g., Gierens et al. 1992; Stoerzer et al. 1996) as well as PDR codes, such as 3D-PDR (Bisbas et al. 2012), which make predictions by postprocessing turbulent ISM simulations. In addition, it is possible that the evolution in some PDRs is driven by nonequilibrium chemistry due to a rapid progression of the ionization front, which can particularly affect the atomic to molecular hydrogen (H I/H_2) transition front (Bertoldi & Draine 1996; Störzer & Hollenbach 1998; Maillard et al. 2021).

Because of the relatively long wavelength of the H I 21 cm line, it is challenging to resolve the structure and dynamics of atomic hydrogen in PDRs with single-dish observations, even for the most nearby regions. Interferometric observations with incomplete u-v spacing coverage, on the other hand, risk resolving out the diffuse emission. To reliably probe the PDR of the reflection nebula/molecular cloud IC 63 in H I we have combined observations of three radio interferometers and single-dish data to ensure both high spatial and spectral resolution and full u-v spacing coverage. We have combined observations from the Giant Metrewave Radio Telescope (GMRT), the Westerbork Synthesis Radio Telescope (WSRT), the Dominion Radio Astrophysical Observatory (DRAO) Synthesis Telescope (ST; Landecker et al. 2000), and the DRAO John A. Galt 26 m single-dish telescope to probe the kinematics and structure of the PDR. Together these observations cover baselines from 23 km (with the GMRT) down to zero-spacing single-dish data (DRAO) and provide the possibility to reach a resolution of 2.″5. In this study we present these interferometric H I 21 cm observations of the IC 63 reflection nebula, complemented with the Stratospheric Observatory for Infrared Astronomy (SOFIA) [C II] 158 μm observations from Caputo et al. (2023, submitted), as well as the H_2 data from Andersson et al. (2013) and Soam et al. (2021a). Since carbon is still ionized when molecular hydrogen

has already formed (Tielens & Hollenbach 1985; Sternberg & Dalgarno 1995), the combined data set allows a study of the PDR structure and dynamics as a function of depth in the PDR. With this high-resolution information, we will investigate whether the atomic to molecular hydrogen transition in a PDR is governed by nonequilibrium chemistry or affected by the 3D turbulent dynamics of the region.

IC 63 is a nebula in the Sh2-185 H II region, which is illuminated and ionized by a B0 IV star, γ Cassiopeia (Karr et al. 2005). This cloud is classified as type-B bright-rimmed cloud by Sugitani et al. (1991). Gaia parallaxes provide a distance of $\lesssim$200 pc to this region which makes it one of the closest H II regions to the Sun (Soam et al. 2021b). Because of its proximity, the interferometric observations reach a high spatial resolution ($\sim 1.5\times10^{-2}$ pc). The nebula has also been extensively studied in many tracers, from the UV (e.g., Witt et al. 1989; France et al. 2005) to the IR (e.g., Fleming et al. 2010; Andrews et al. 2018) and mm-waves (e.g., Jansen et al. 1994; Soam et al. 2021b).

The atomic hydrogen emission from IC 63 has previously been studied by, e.g., Blouin et al. (1997), using the DRAO ST outside Penticton, British Columbia. However, even with the 604.3 m maximum fully sampled baseline of the DRAO ST, the angular resolution at 1.42 GHz of H I data only reaches $1'\times 1\farcm14$ for IC 63 (Blouin et al. 1997). For comparison, the SOFIA/upGREAT [C II] maps obtained by M. Caputo et al. (2023, in preparation) have a beam size of $\sim14''$ and the GBT/ARGUS CO($J=1$–0) observations (in a forthcoming paper) have a beam size of $8''$. Therefore high-sensitivity and high-resolution observations of the region require more extensive arrays.

2. Observations and Data Reduction

Because of the small angular size of the IC 63 PDR, very high spatial resolution is needed to analyze the nebula. We therefore combine radio interferometry from GMRT in India, WSRT in the Netherlands, and DRAO ST in British Columbia, Canada. To ensure full u-v plane coverage, especially at short spacings, single-dish observations using the DRAO 26 m antenna were also added.

2.1. GMRT Observations

The GMRT H I observations were taken in January 2017. These used the GMRT Software Backend (Roy et al. 2010) with 512 channels across a bandwidth of 2.083 MHz, giving a channel separation of 0.86 km s^{-1}. The data were reduced and imaged using AIPS (Greisen 2003) with a restoring beam of $8\farcs5$.

2.2. WSRT Observations

The WSRT H I observations were taken over 4 × 12 hr with the legacy WSRT system in the 36 m+54 m+72 m+90 m configurations in December 2008 using 1024 channels over a bandwith of 2.5 MHz, giving a channel separation of 0.52 km s^{-1} and an angular resolution of $15\farcs2\times13\farcs4$. They were reduced and imaged using standard procedures in MIRIAD using the CLEAN algorithm (Sault et al. 1995). To check whether the clumpiness of the HI in the resulting image was a CLEAN artifact, the data was also imaged using the MAXEN algorithm to carry out a maximum entropy deconvolution, resulting in a virtually identical image.

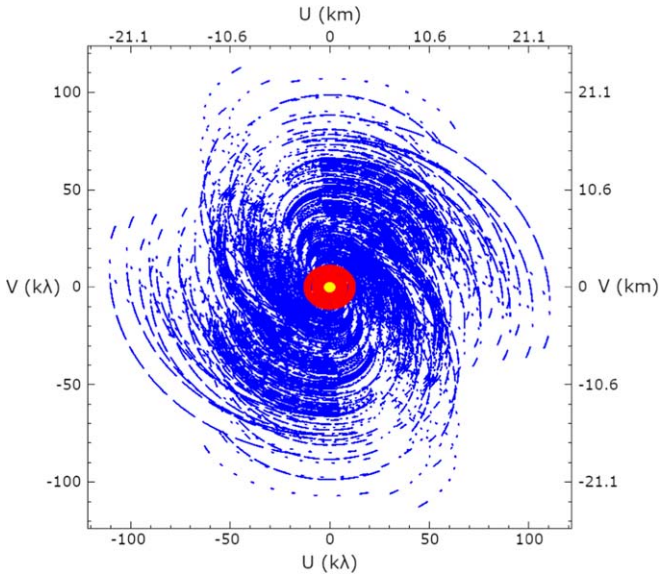

Figure 1. Coverage of the UV plane for the IC 63 observations by the different observatories. Blue is GMRT, red is WSRT, and yellow is CGPS.

Table 1
Baselines for the Different Data Sets

Data Set	Baselines
CGPS	0–26 m+12.9–604.3 m
WSRT	36 m–2.7 km
GMRT	100 m–26 km

2.3. DRAO Observations

The DRAO H I data utilized here were originally acquired as part of the Canadian Galactic Plane Survey (CGPS; Taylor et al. 2003, 2017). Those observations were taken in Phase I of the CGPS in 1995–2000 and include single-dish observations taken to fill in the zero-spacing data. The observations cover 272 channels with a channel separation of 0.82 km s^{-1} and an angular resolution of $1'\times1\farcm14$.

2.4. H I Data Reduction

The three data sets were combined linearly in the Fourier domain using the IMMERGE task in MIRIAD (Sault et al. 1995), using the CLEANed and primary beam corrected WSRT and GMRT images and a UV range for relative flux calibration of 150–500 m, which is present and well sampled in all three data sets (see Table 1; Figure 1). Prior to combination, the WSRT and DRAO images were regridded onto the spatial and spectral grid of the GMRT data. This gives a final combined data set with the $8\farcs5$ angular resolution and the 0.86 km s^{-1} spectral resolution of the GMRT data. In order to improve the signal-to-noise ratio (S/N) of the data and work with a resolution similar to the [C II] data, we decided to proceed with a data cube smoothed to an angular resolution of $15''$.

2.5. SOFIA Observations

The [C II] fine-structure line at 158 μm was observed with the upGREAT receiver (Heyminck et al. 2012; Risacher et al. 2016, 2018) onboard SOFIA (Young et al. 2012). The data is part of SOFIA project 05_0052 (PI: B-G Andersson). The IC

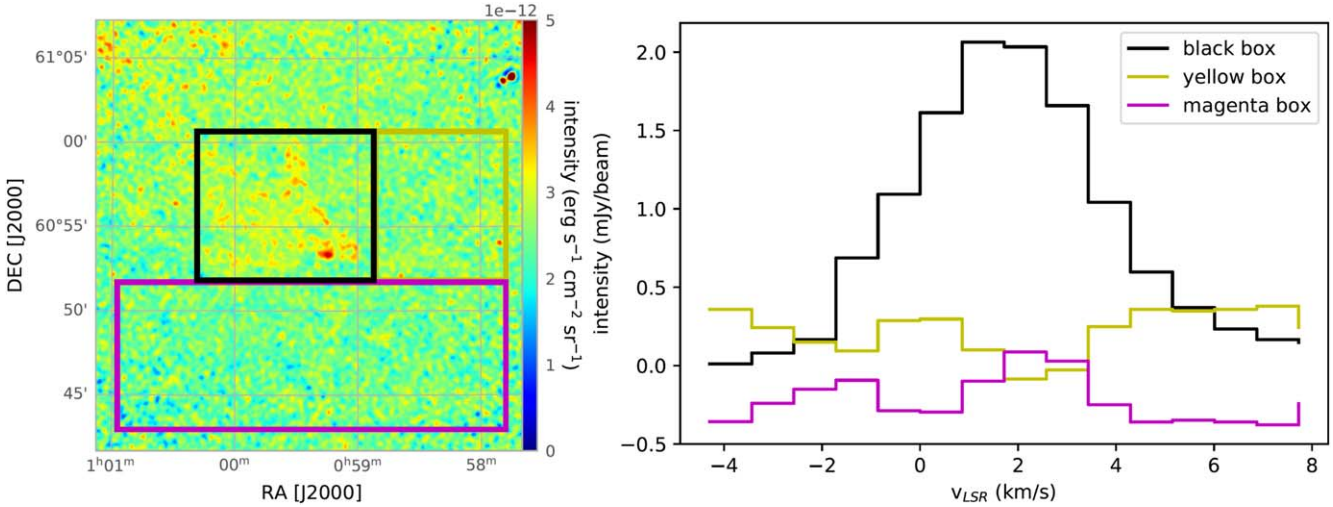

Figure 2. Left: H I integrated intensity map (without background subtraction) of the IC 63 region. The yellow and magenta boxes indicate the regions used to make an average spectrum for background subtraction. The black box indicates the region associated with IC 63. Right: the spectra from the corresponding colored boxes on the left after background subtraction. The emission from IC 63 (black) has a clearly defined profile while the background regions (yellow and magenta) are relatively close to the baseline.

63 nebula was mapped in the total power on-the-fly mode (TP OTF), reaching an angular resolution of 15″. The observations were calibrated with the GREAT calibration software (Guan et al. 2012) and the main beam efficiencies for the 7 different pixels of upGREAT vary between 0.59 and 0.68. To create the final data cubes, a second order baseline was fitted to the data with CLASS[8] and the data was spectrally smoothed to a resolution of 0.4 km s^{-1}. Caputo et al. (2023, submitted) will present a more detailed description of the [C II] observations and data reduction.

3. Results

3.1. Galactic Background Removal

Since IC 63 is located relatively close to the Galactic plane ($b \approx -2°$), the observed H I spectra are heavily confused/contaminated by background emission (Taylor et al. 2003; McClure-Griffiths et al. 2005). In order to obtain the actual emission from IC 63, the galactic background has to be removed. To do so, we take a relatively simple approach where we define an average H I background spectrum from regions of the data cube that do not contain emission associated with IC 63. We chose this approach because IC 63 is already clearly visible in the available data cube and the method gives excellent control on what is removed to isolate the emission associated with IC 63.

Two rectangular regions were used to define the average background spectrum for IC 63. These two regions are indicated by the yellow and magenta boxes presented in Figure 2. They are the only two regions that do not contain emission from IC 63 (which is located in the black box in Figure 2). For the rest of the map, i.e., the northeast of the map, it is not certain whether there is a contribution from IC 63 or IC 59 in the northwest corner of the map. As a result, these other regions are not taken into account for the background subtraction. Subtracting the average background spectrum in each spatial pixel of the full data cube then creates the data cube that contains the emission associated with IC 63. The resulting H I integrated intensity map is shown in Figure 3 and the resulting average spectrum for IC 63 is presented in the right panel of Figure 2. This shows a Gaussian line profile. From this point forward, we will work with the background-subtracted data unless mentioned otherwise.

3.2. The Integrated Intensity Map

The integrated intensity map of the H I emission toward IC 63 is presented in Figure 3. Overall, it shows the same morphology for IC 63 that is also seen in, e.g., the WISE maps (e.g., Soam et al. 2017). When looking in more detail, it shows a bright clump and a ring-like morphology at the southwest head of the region with further H I emission in elongated structures pointing toward the north, northeast, and east of the map (which we here also call legs). The H I emission in these legs show a quite pronounced clumpy morphology as well. The [C II] map is more limited in size and only covers the head of IC 63. Inspecting the [C II] emission in Figure 3 shows that the brightest emission is located toward the head of the nebula with lower brightness emission extending further along the start of the legs in the region. It is interesting to note that there are regions in Figure 3 with [C II] emission that do not have a counterpart in H I emission.

We do not expect that the clumpiness of the H I emission is the result of filtering during the data reduction. Reducing the observations using the CLEAN technique, which tends to create clumpy structures, and the MEM technique, which produces smoother structures, we find that the clumpy structure of the H I emission is maintained in both. This is shown in Appendix. A. Inspecting the zoom into the tip of IC 63 in Figure 3, we also find that the H I emission shows a remarkable ring-like feature with an intensity drop in the middle. This behavior is not seen in [C II], see Figure 3, which rather shows bright emission toward the front of the PDR followed by a gradually decreasing intensity toward the back.

Given the relatively limited S/N of the H I observations, it could be suggested that the clumpiness of the H I data is simply due to the noise. To assess this, we determined the noise in the lower region of the integrated map without any known emission (i.e., the yellow and magenta boxes in Figure 2).

[8] https://www.iram.fr/IRAMFR/GILDAS/doc/html/class-html/class.html

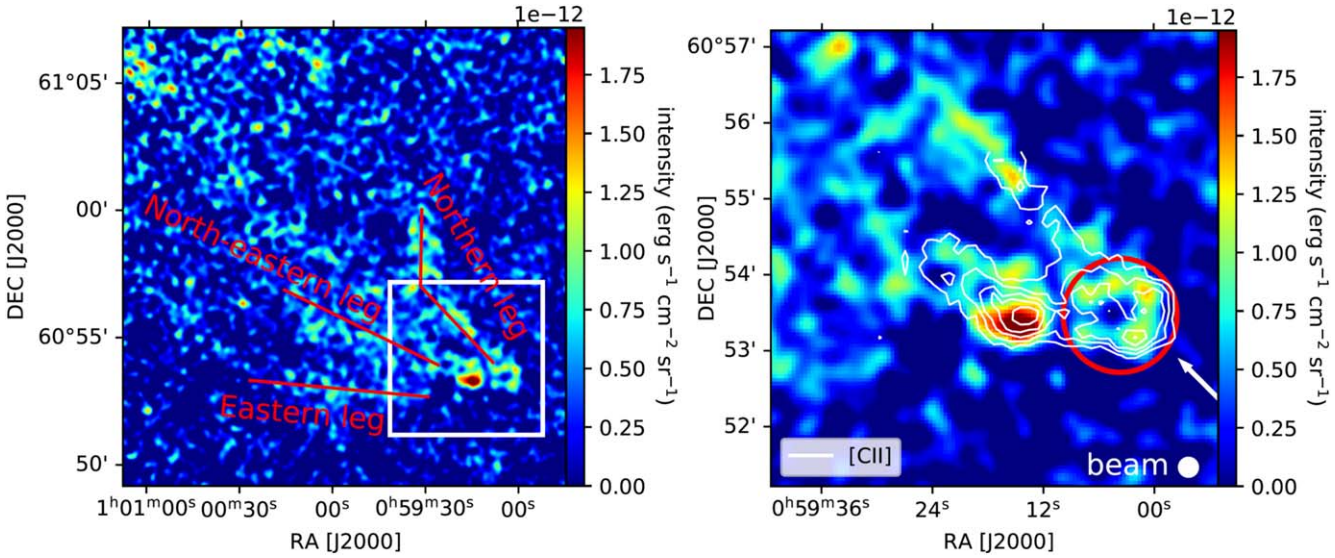

Figure 3. Left: the H I intensity map of IC 63 that is obtained from the background-subtracted data cube. The white box outlines the zoomed-in region presented on the right. The red lines indicate the three legs visible in H I that are connected to the tip of IC 63 with their names. Right: a zoom into the brightest region of H I intensity map with the [C II] intensity contours overlaid (starting at 10^{-4} erg s^{-1} cm^{-2} sr^{-1} with increments of 5×10^{-5} erg s^{-1} cm^{-2} sr^{-1}). The red circle highlights the circular morphology seen in H I toward the tip of IC 63. The white arrow indicates the direction of the incident radiation from γ Cas. The full white circle indicates the 15″ beam size of the H I data.

This indicates a noise rms of 3.3×10^{-13} erg s^{-1} cm^{-2} sr^{-1}. However, inspecting the map we identify several clumps/locations, including the ring, that have a contrast above 10^{-12} erg s^{-1} cm^{-2} sr^{-1} (i.e., higher than 3σ) compared to their surroundings. Even though the limited S/N in the integrated map might have some effect, we find that several clumps should not be a S/N effect and therefore we are relatively confident that the H I emission really is rather clumpy. More sensitive observations in the future should allow to explore this clumpiness with greater confidence.

3.3. The Kinematics of IC 63

The channel maps in Figure 4 provide a view of the H I kinematics in IC 63. At the most blueshifted velocities ($\lesssim$0 km s^{-1}), the most eastern part of IC 63 is prominent. At slightly more redshifted velocities (0.8–1.7 km s^{-1}), the northern leg becomes bright with the northeastern leg between 0.8 and and 3.4 km s^{-1}. This clearly demonstrates that the different legs of IC 63 are velocity-coherent gas structures in the region.

For a more detailed look into the kinematics of IC 63, we also made several position–velocity (PV) diagrams that cut through the IC 63 region. These PV diagrams go along and perpendicular to northeastern and northern legs, and across the ring and brightest H I clump. The resulting PV diagrams, overlaid with [C II] contours are presented in Figure 5. Focusing first on the H I emission alone, it is observed that there is a velocity gradient from more blueshifted to more redshifted along the northern leg (PV 3) and toward the northeast from the tip (PVs 5 + 1). In the cut perpendicular to the legs (PV 2), a hint of the velocity gradient west to east is seen in H I. It is however tentative due to the limited spectral resolution and relatively high noise in the H I data. Lastly, the cut through the ring at the tip of the nebula shows a velocity gradient from south (1–2 km s^{-1}) to the north (0 km s^{-1}) (see PV 6) while the clump to the east does not show any clear gradient (see PV 4).

When comparing the H I and [C II] kinematics—the [C II] kinematics are presented and studied in more detail in Caputo et al. (2023, submitted)—both differences and similarities are observed. The kinematics of the legs in H I and [C II] appear to show the same behavior, see Figure 5, even though some regions that are detected in [C II] are not detected in H I which is the result of the clumpy H I structure. The gradient from west to east (in PV 2 of Figure 5) that was found in the H I channel maps is however not really clear in [C II]. Most remarkable is probably the difference of the centroid velocity for H I and [C II] toward the head of IC 63. Figure 5 shows that the [C II] velocity field remains constant toward the ring whereas a gradient is observed in the H I emission. This velocity difference of both lines is confirmed when fitting the [C II] and H I data with a single Gaussian velocity profile, which finds velocity difference of the order of 1–2 km s^{-1}, see Figure 6. From this figure it is observed that [C II] is predominantly blueshifted with respect to H I in most parts of the ring while it is slightly redshifted with respect to H I in the bright clump to the east of the ring (in particular at the edge of the clump). Note that there is some uncertainty on the fitted central velocities because of the low S/N of the H I data. However, the velocity typically has an uncertainty of 0.1 km s^{-1} and does not go over 0.2 km s^{-1}. The velocity shifts thus appear to be statistically significant.

4. Discussion

4.1. The Dynamic Evolution and Timescales of IC 63

The three major legs, defined in Figure 3, of IC 63 are each seen at a different velocity, confirming they are coherently moving substructures of IC 63. From the H I channel maps it was observed that the most eastern leg is the most blueshifted. This leg is proposed to be the closest to us (Andersson et al. 2013), which would imply that the different legs are currently being dispersed. Based on the 0.5 pc physical size of the H I legs at a distance of $\sim$170 pc (van Leeuwen 2007), the velocity difference of $\sim$1–2 km s^{-1} implies that IC 63 might be fully dissolved in $\leqslant$0.5 Myr. Interestingly, this is similar, and even

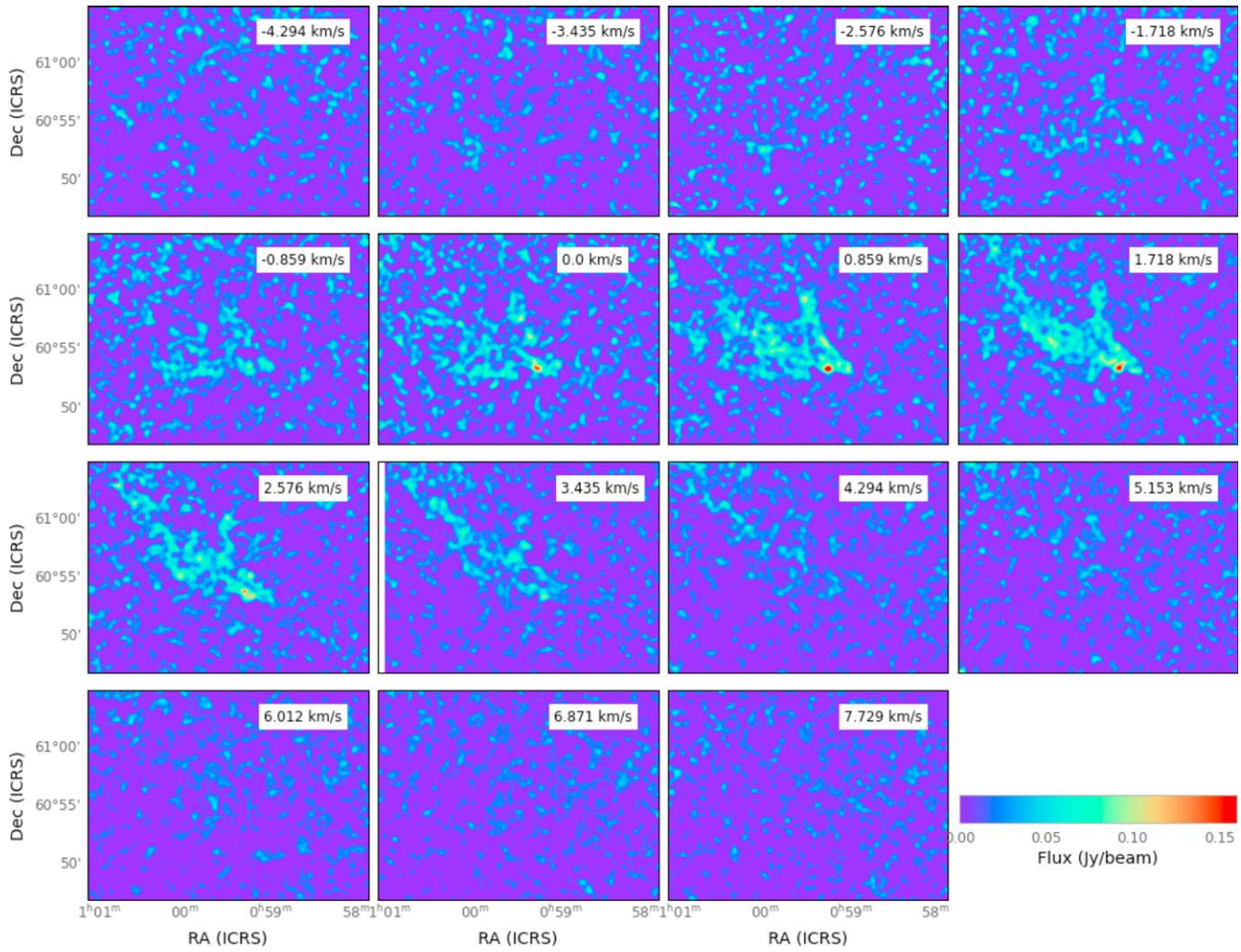

Figure 4. Channel maps between –4.3 and 7.7 km s^{-1} of the IC 63 region in steps of ∼0.8 km s^{-1}.

slightly shorter, than the dispersal timescales that are found with [C II] for denser regions around high-mass star formation (Tiwari et al. 2021; Bonne et al. 2022). As IC 63 is likely at a more evolved stage where most of the dense gas has already been dispersed, this indicates that the more diffuse gas around star-forming regions can be dispersed on relatively similar timescales. Another interpretation for this velocity field could be a relatively rapid rotational motion of the legs if IC 63 is spinning, although it is unclear what would drive the spinning of this region. It is also observed that the legs to the north of the map are found to be generally more redshifted in Figure 4. This velocity gradient could be associated with the dispersal of the region, but it is difficult to reach a firm conclusion.

Based on Figure 6 we noted that H I and [C II] show up at slightly different velocities, in particular toward the bright clump and ring at the head of IC 63. As H I is expected to trace the outer regions of the PDR compared to [C II], because H_2 can form while carbon is still ionized (Tielens & Hollenbach 1985; Sternberg & Dalgarno 1995), this suggests that there is a velocity gradient over the PDR. The bright PDR in IC 63 is thus a dynamic structure with local velocity differences up to 1 km s^{-1}. As these clumps have a size of only 0.05 pc, the structure of these bright PDRs would thus be changing on a relatively short timescale of only $\sim 5 \times 10^4$ yr. The potential effect of these dynamics on the chemical structure of the PDR will be discussed in more detail in the next section.

4.2. The Ring and Clumpy PDR Structure of H I in IC 63

In order to assess the emission profile of the H I ring-like structure at the tip of the nebula, we created eight radial cuts through the ring. The resulting H I profiles as a function of radius are presented in Appendix. B. This confirms an axial symmetry of the emission with the peak emission in the 8 cuts only varying within 30% among the different profiles, which is expected based on the noise rms. The dip toward the center of the ring is however larger than 3× the noise rms. In Appendix. B it is also verified that the observed ring-like morphology is retrieved from the data of the different interferometers. With this evidence of a ring-like structure, we folded these 8 H I profiles (i.e., average the profile at negative offset with the profile at positive offset) and then averaged all eight profiles into a single H I emission profile for the ring. This average emission profile, fitted with a Gaussian distribution, is presented in Figure 8. The central intensity is 1.4×10^{-13} erg s^{-1} cm^{-2} sr^{-1} and the peak intensity of the ring is 9.3×10^{-13} erg s^{-1} cm^{-2} sr^{-1}, resulting in a peak to center ratio of ∼7. The question arises whether this ring-like structure is the result of self absorption or rather a result of the hydrogen chemistry or

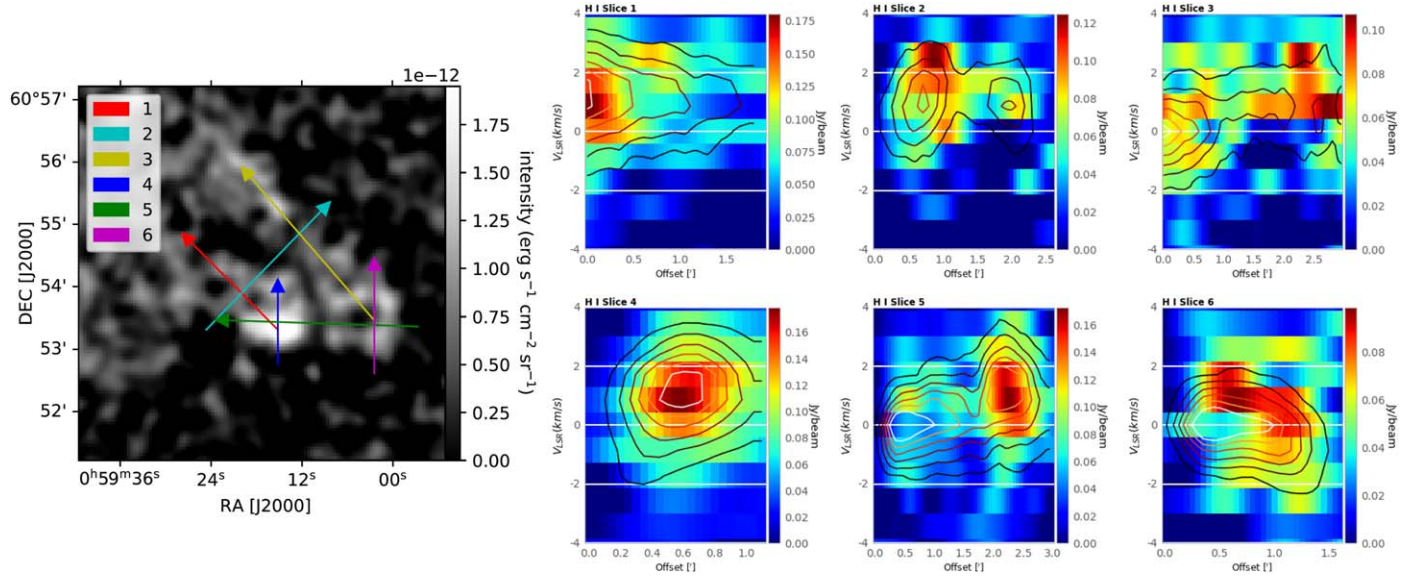

Figure 5. Left: the H I moment zero map for IC 63 with the colored arrows indicating the cuts that were made to construct position–velocity (PV) diagrams on the right. Right: the H I PV diagrams along the axes/arrows indicated in the figure on the left. The contours indicate the corresponding [C II] PV diagrams starting at 2 K with increments of 2 K. The darkest contours indicate the weakest emission and the white contour indicates the brightest emission.

dynamics in the PDR. Investigating the individual spectra for self absorption unfortunately does not provide conclusive insight because of the limited S/N for the currently available observations. We can, however, constrain this possibility, as well as chemical effects, with a toy model. This model assumes a spherical geometry for the optically thin atomic hydrogen that is organized in a shell with a constant spin temperature, see Figure 7. In the interior of the shell we consider either the lack of H I emission due to chemistry, e.g., the formation of H_2, which can be supported by the H_2 fluorescence observations in Andersson et al. (2013), or the presence of cold atomic H I self-absorbing (HISA) gas. With this toy model we can use the observed size and thickness of the ring, and compare it to the ratio of brightness temperature at the center and rim. We can also evaluate whether the required H I absorbing layer is consistent with the A_V (i.e., extinction in the V band) of IC 63.

If we assume that the shell is basically devoid of H I, due to the formation of H_2, then the ratio at the center and the rim will be proportional to the path lengths through the shell, see Figure 7. If we designate the inner and outer radii of the shell r_i and r_o, the radial path length at the center of the shell is simply $C = 2{\cdot}(r_o - r_i)$ and the distance from the center to the middle of the rim is $\frac{1}{2} \cdot (r_o + r_i)$. The path length through the middle of the shell is then $S_{\rm cent} = 2 \cdot \sqrt{r_o^2 - 0.25 \times (r_o + r_i)^2}$. For further use in equations we here define the size (Δ) and thickness (δ) with the following relations:

$$\delta = r_o - r_i;\ \Delta = \frac{1}{2} \cdot (r_o + r_i). \tag{1}$$

The largest pencil-beam column density through the shell occurs at $r = r_i$ with a resulting path length ratio

$$\frac{S_{\rm long}}{C} = \frac{\Delta + \frac{\delta}{2}}{\delta} \sqrt{1 - \left(\frac{\Delta - \frac{\delta}{2}}{\Delta + \frac{\delta}{2}}\right)^2}. \tag{2}$$

However, we are comparing to observations with a finite-sized beam, and the predicted shell intensity profile is not symmetric at the peak (see Figure 14 in Kabanovic et al. 2022). This can thus affect the observed S/C ratio and slightly shift the radius of the observed peak emission in a nontrivial way. Therefore, we also use the center path length through the shell, which gives

$$\frac{S_{\rm cent}}{C} = \frac{\sqrt{\left(\Delta + \frac{\delta}{2}\right)^2 - \Delta^2}}{\delta}. \tag{3}$$

This provides an expected range of observed S/C ratios that accounts for the fact that we are observing at finite resolution.

Figure 8 shows that $\Delta \approx 25\farcs2$ and $\sigma_\delta \approx 11\farcs4$ (σ_δ is the observed width of the shell). Deconvolving the shell-width with the $6\farcs4$ beamwidth (=$\mathrm{FWHM_{beam}}/2\sqrt{2\ln 2}$ with $\mathrm{FWHM_{beam}} = 15''$), σ_δ becomes $9\farcs4$. The width of the shell is probably better approximated by the FWHM, rather than the Gaussian width σ which yields $\delta \approx 22\farcs1$. Inserting these values into Equations (2) and (3), we find path length ratios S/C in the range of 1.2–1.5. However, the observed brightness temperature ratio for the shell and center of the ring is $T_S/T_C = 6.9 \pm 1.5$, which is significantly larger than the geometric ratio. It might thus be that the H I shell is not spherical, see e.g., Figure 7, or that there is HISA at the center of the ring.

To calculate the potential cold H I column density, and compare it to the visual extinction in the cloud, we calculate the HISA optical depth

$$\tau_{\rm HISA}(v) = -\ln\left(1 - \frac{T_{\rm on-off}(v)}{T_{\rm HISA} - pT_{\rm off}(v) - T_{\rm cont}}\right) \tag{4}$$

where $T_{\rm on-off}$ is the difference between the HISA ($T_{\rm on}$) and background ($T_{\rm off}$) brightness, $T_{\rm HISA}$ is the HISA temperature, p a dimensionless parameter in the range [0–1], which accounts for foreground emission, and $T_{\rm cont}$ the continuum brightness (which we ignore here). We here use $p = 1$ which assumes no foreground emission for $T_{\rm off}$. From this it is then possible to

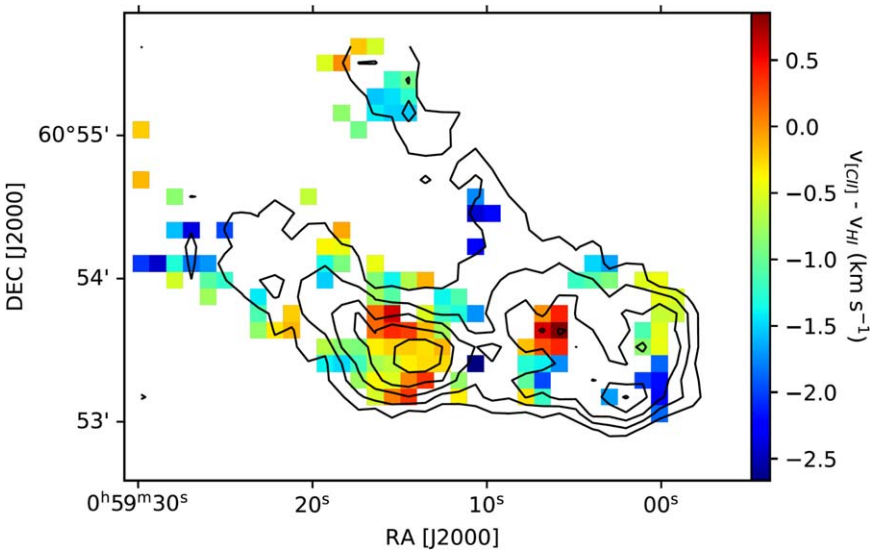

Figure 6. The difference in central velocity of the emission in [C II] (Caputo et al. 2023, submitted) and H I at the locations where both lines are detected. The black contours indicate the integrated [C II] emission starting at 10^{-4} erg s^{-1} cm^{-2} sr^{-1} with increments of 5×10^{-5} erg s^{-1} cm^{-2} sr^{-1}.

calculate the HISA column density using (Wilson et al. 2009)

$$N_{\rm HISA}\ [{\rm cm}^{-2}] = 1.8224 \times 10^{18}\, T_{\rm HISA}\ [K] \times \int \tau_{\rm HISA}(v) dv\ [{\rm km\ s}^{-1}]. \quad (5)$$

Here, we are however hampered by the noisy spectra. Therefore, we assume a constant $\tau_{\rm HISA}$ with $T_{\rm on-off} = -137$ K and $T_{\rm off} = 159$ K. $T_{\rm on-off}$ and $T_{\rm off}$ were calculated based on the central and peak intensity of the ring mentioned above with an assumed FWHM of 2 km s^{-1}. Assuming $T_{\rm HISA} = 20$ K this gives rise to a required $N_{\rm HISA}$ values of 3×10^{20} cm^{-2}. For $T_{\rm HISA} = 10$ K this drops to 9×10^{19} cm^{-2}, but at $T_{\rm HISA} = 30$ K no solution can be found. For HISA temperatures of only 20 K or less it is thus possible to find a solution. In addition, the column density associated with HISA is well below the total column density at the tip of IC 63 ($A_V \approx 2$ (Van De Putte et al. 2020), accounting for foreground and background extinction). With an $A_V \approx 2$, or $N_{\rm H} \approx 4.4 \times 10^{21}$ cm^{-3} (using Güver & Özel (2009)), about 2%–7% of the gas in the line of sight would be associated to HISA. However, it has to be noted that these are significant column densities for such cold HISA (Wang et al. 2020; Kabanovic et al. 2022; Seifried et al. 2022). In addition, for a path length of 0.05 pc the typical density would be of the order of 0.6–3 $\times 10^3$ cm^{-3} which is relatively high. It is thus possible to explain the ring morphology in IC 63 with H I self absorption, but the HISA conditions would have to be quite extreme compared to typical values in the Galactic ISM. More sensitive observations will be able to properly address this question.

Another option to explain the ring as well as the clumpy structure of H I in the PDR would be a chemical effect that removes the presence of a layered PDR. Work by Störzer & Hollenbach (1998) proposed a criterion $\chi/n < 0.2 v_{\rm IF}$[9] where a PDR is dominated by nonequilibrium chemistry that removes the presence of a H I/H_2 transition front. The recent semianalytical solution by Maillard et al. (2021) proposes a more involved criterion for the transition to nonequilibrium PDR chemistry and no clearly defined H I/H_2 transition front (see their Equation (16)). To examine the potential role of nonequilibrium chemistry in the IC 63 PDR, we compute the typical ionization front velocity ($v_{\rm IF}$) for the head of this region using

$$v_{\rm IF} = \frac{n_e}{n_{\rm PDR}} v_{\rm II} \quad (6)$$

with n_e the electron density on the H II side of the ionization front, a velocity $v_{\rm II} \approx c_{\rm II} \approx 10$ km s^{-1} (i.e., the sound speed of the ionized gas; Störzer & Hollenbach 1998) and $n_{\rm PDR}$ the density of the PDR. To calculate the electron density (n_e), we use the 1.4 GHz NRAO VLA Sky Survey radio continuum data (Condon et al. 1998). At the tip of IC 63, we typically find values of 0.05 Jy beam^{-1} with a beam size of 45″. Since the radio continuum spectral index analysis from Blouin et al. (1997) indicates that the emission at 1.4 GHz is optically thin in IC 63, we can use

$$\left(\frac{\rm EM}{\rm pc\ cm^{-6}}\right) = 3.217 \times 10^7 \left(\frac{F_\nu}{Jy}\right)\left(\frac{\nu}{GHz}\right)^{0.1}\left(\frac{T_e}{K}\right)^{0.35}\left(\frac{\theta_{\rm source}}{\rm arcsec}\right)^{-2} \quad (7)$$

taken from Schmiedeke et al. (2016) to calculate the emission measure (EM). Here, F_ν (=0.05 Jy) is the flux density, T_e (=8000 K) the electron temperature, ν (=1.4 GHz) the observed frequency, and $\theta_{\rm source}$ (=45″) the studied aperture. This results in EM = 1.9×10^3 pc cm^{-6}. Using a size of 0.05 pc results in $n_e = 2.0 \times 10^2$ cm^{-3}. To calculate the density in the PDR, Van De Putte et al. (2020) found an $A_V \approx 2$ for IC 63. Combining this with a typical size of 0.05 pc for the clumps gives a proton density $n_{\rm H} = 2.8 \times 10^4$ cm^{-3} using the relation from Güver & Özel (2009) that links A_V to column density. Combining this gives $v_{\rm IF} = 7.0 \times 10^{-2}$ km s^{-1}. To determine whether the PDR is governed by nonequilibrium processes we have to estimate the

[9] With χ the FUV field strength (Draine 1978), n the density and $v_{\rm IF}$ the ionization front (IF) velocity.

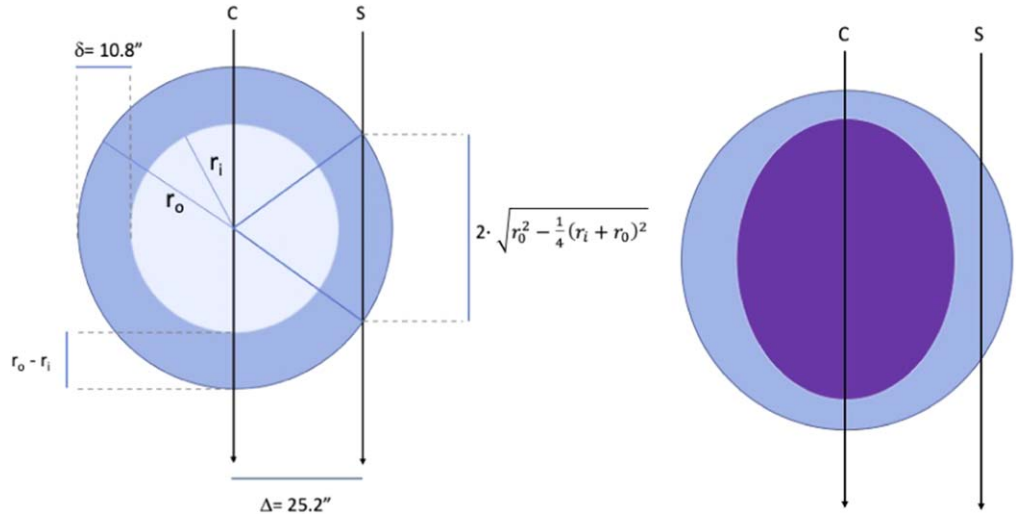

Figure 7. Left: the geometry of a simple model to estimate whether the observed H I ring is the projection of a spherical ring (see Equations (2) and (3)). In this specific schematic presentation, S corresponds to the path length through the center of the shell (S_{cent}). If we assume that all of the H I emission is optically thin, we can compare the geometric ratio of ring size and rim/shell thickness with the ratio of the related brightness temperatures. The observed ring radius is $\Delta = 25\farcs2$ and the shell thickness (FWHM) yields $\delta = 22\farcs1$. Right: the observed intensity ratio could be recovered from this model if we assume that the shell is anisotropic, and/or that the center of the region is filled with cold, self-absorbing (HISA) gas.

FUV field strength. For the FUV field strength, the original literature proposes a value of $\chi \approx 6 \times 10^2$ (Jansen et al. 1994) at a distance of 1.3 pc from the ionizing star γ Cas. We verified this value, using a distance of 1.3–2 pc from γ Cas (Caputo et al. 2023, submitted) with the method presented in Bonne et al. (2020). This directly calculates the FUV field strength at a specific distance from an OB star (or cluster) using the emitted radiation as a function of wavelength from the OB stars in the Kurucz (1979) models. This results in $G_0 = 1.1$–2.6×10^2 (with $G_0 = 1.7\chi$, this leads to $\chi = 0.65$–1.5×10^2), which is significantly lower than the prediction by Jansen et al. (1994). However, the value calculated here is consistent with more recent work by Andrews et al. (2018) who proposed an FUV field strength $\chi \approx 90$ and Soam et al. (2021a) who found $\chi = 0.6$–2.4×10^2. To investigate this in more detail, we use the [C II] intensity presented in Caputo et al. (2023, submitted), which typically is 2.5–3.0 $\times 10^{-4}$ erg s^{-1} cm^{-2} sr^{-1}, and the PDR Toolbox (Pound & Wolfire 2008, 2023). At densities of 1–5 $\times 10^4$ cm^{-3} this [C II] intensity corresponds to a typical FUV field of $\chi = 0.6$–2.0×10^2. This is consistent with the estimate based on the method in Bonne et al. (2020). Using the calculated v_{IF}, the prescription by Störzer & Hollenbach (1998) provides a critical $(\chi/n)_{crit} = 1.4 \times 10^{-2}$ and the prescription by Maillard et al. (2021) gives $(\chi/n)_{crit} = 2.4 \times 10^{-3}$. Using the determined $\chi = 0.6$–2.0×10^2 range from the [C II] observations gives $\chi/n = 2.1$–7.1×10^{-3} for IC 63. The results based on both criteria provide different conclusions. The Maillard et al. (2021) criterion suggests there likely still is a H I/H_2 transition front whereas the Störzer & Hollenbach (1998) criterion suggests IC 63 no longer has a H I/H_2 transition front, which might provide an explanation for the more complex or clumpy H I structure. However, it has to be noted that the Maillard et al. (2021) solution should be the more accurate one as it includes the dynamics induced by the photoevaporation and dust shielding (Sternberg et al. 2014).

A last thing to consider is the dynamics in the PDR itself which might be significant when considering the apparent 1 km s^{-1} offset in velocity between H I and [C II], in particular toward the tip of the region, in Figure 6. In the previous section we obtained a dynamical timescale of 5×10^4 yr for the PDR which we can compare with the H_2 dissociation timescale. Based on Draine & Bertoldi (1996) and Störzer & Hollenbach (1998), this is given by

$$t_{H_2} \approx 0.6 \frac{N(H_2)^{3/4}}{\chi} \text{s}. \quad (8)$$

Using $N(H_2) = 0.5 \times 10^{21}$ cm^{-2} (Störzer & Hollenbach 1998) and $\chi = 0.6$–2.0×10^2 results in a dissociation timescale of 0.3–1.0 Myr. It thus appears that the dynamical timescale is significantly shorter than the H_2 dissociation timescale. As a result the dynamics in the PDR can reorganize the internal structure and so remove a plane-parallel H I/H_2 structure, which could explain the observed clumpy H I structure.

5. Conclusions

We have presented combined interferometric H I observations from the GMRT, WSRT and DRAO of IC 63 with an effective angular resolution of 15″, which allows to resolve the structure of the PDR in IC 63. These observations are further complemented with SOFIA [C II] data. To properly analyze the H I observations at the low Galactic latitude of IC 63 ($b = -2$), we subtract the galactic background from the spectrum using nearby regions devoid of H I emission associated with IC 63. Although the S/N is somewhat limited we conclude that the H I structure of IC 63 appears to be clumpy, and that the tip of IC 63 appears to have a ring-like morphology in H I. With analytical models, we show that this ring-like structure is likely not the projection of an unfilled spherical shell. However, more sensitive observations with new and future observatories can help to confirm these results and explore them in further detail. We also obtain a view on the dynamics. This shows dynamic structure with $\Delta v \approx 1$ km s^{-1} inside the tip of the PDR. In addition, the full region consists of several legs that appear to

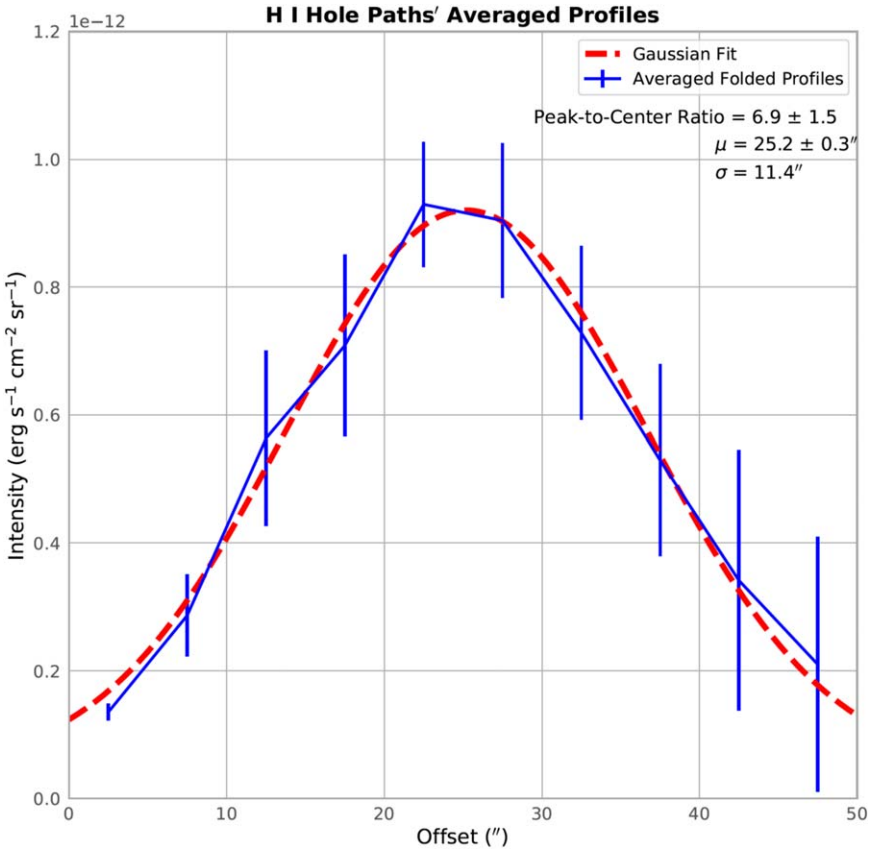

Figure 8. The average H I emission profile of the ring as a function of the offset from the center of the ring with a Gaussian profile fitted to it (red dashed line). The error bars indicate the standard deviation of the emission over the ring at each offset.

be moving apart. This suggests that IC 63 will completely disperse within less than 0.5 Myr.

Analyzing the H I spectra and PDR characteristics, we conclude that the dynamical timescale in the PDR is too short for there to be a plane-parallel H I/H_2 structure, which could explain the clumpy H I structure. The S/N is not sufficient to conclude on the contribution of HISA to the spectra, but if the HISA temperature is below 20 K then HISA can contribute to the apparent clumpy H I structure. We also investigated whether the ionization front velocity leading to nonequilibrium chemistry could explain the clumpy structure. Different prescriptions for the transition to nonequilibrium chemistry due to the ionization front velocity lead to different conclusions, but the most recent and accurate prescription by Maillard et al. (2021) concludes that nonequilibrium chemistry should not play a major role. We thus tentatively propose that the apparent clumpy H I PDR structure is predominantly explained by the short dynamical timescale in the PDR, but it cannot be excluded that different mechanisms contribute to this observed clumpy H I structure.

We thank G. Barentsen for fruitful exchange on the use of the IPHAS data set. We acknowledge the professional and patient support of the WSRT staff, in particular Gyula Jozsa and Adriaan Renting. We thank the staff of the GMRT that made these observations possible. GMRT is run by the National Centre for Radio Astrophysics of the Tata Institute of Fundamental Research. This research used the facilities of the Canadian Astronomy Data Centre operated by the National Research Council of Canada with the support of the Canadian Space Agency. L.B. was supported by a USRA postdoctoral fellowship, funded through the NASA SOFIA contract NNA17BF53C. B-G A., A.S., and J.K. gratefully acknowledge the support from the National Science Foundation (NSF) under grant AST-1715876 to USRA. K.K. and J.Y., gratefully acknowledge the support from NSF under grant AST-1715060 to SCU. J.Y. was supported by a Fox Fellowship from Santa Clara University. R.M. acknowledges support from the National Radio Astronomy Observatory (NRAO). The National Radio Astronomy Observatory is a facility of the National Science Foundation operated under cooperative agreement by Associated Universities, Inc. Based, in part, on observations made with the NASA/DLR Stratospheric Observatory for Infrared Astronomy (SOFIA). SOFIA is jointly operated by the Universities Space Research Association, Inc. (USRA), under NASA contract NAS2-97001, and the Deutsches SOFIA Institut (DSI) under DLR contract 50 OK 0901 to the University of Stuttgart.

Facilities: GMRT, WSRT, DRAO, SOFIA(upGREAT), CFHT(WIRCam), CADC.

Software: astropy (Astropy Collaboration et al. 2013), MIRIAD (Sault et al. 1995), AIPS (Greisen 2003).

Appendix A
CLEAN versus MEM Reduction

Figure 9 displays the moment zero map for the H I emission between –2.5 and 4.5 km s^{-1}, which is not background subtracted, when reduced using the MEM technique (left) and the CLEAN technique (right). Both methods create a very

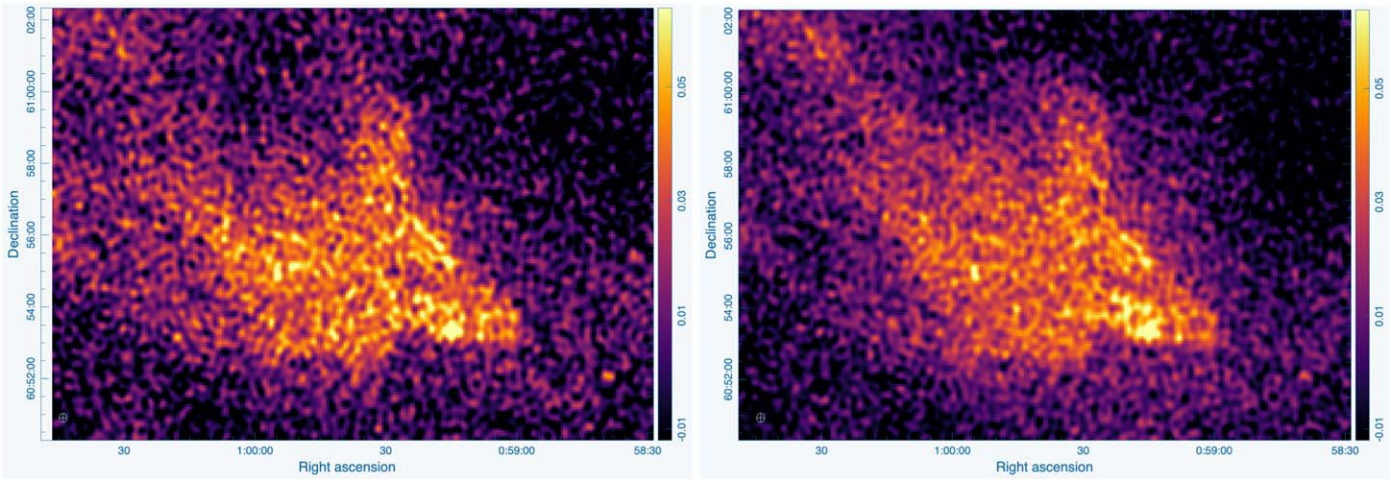

Figure 9. Left: the moment zero map for IC 63 between −2.5 and 4.5 km s^{-1} obtained using the MEM reduction technique. Right: the same using the CLEAN reduction technique, showing a similar clumpy morphology.

similar map which indicates that the clumpy morphology for the region is not an artifact.

Appendix B
The Individual H I Profiles and Spectrum Over the Ring

To obtain a better view of the ring-like feature, we created eight cuts through the ring with in steps of 20°, which is shown in Figure 10. The resulting profiles along the cut are presented in Figure 10. The center was defined by making that the offset from the center to the maximum intensity is equal in the positive and negative direction along the vertical and horizontal axes. Within a typical offset of ± 40″, the profiles show similar behavior with peak values varying between 0.7×10^{-12} and 1.4×10^{-12} erg s^{-1} cm^{-2} sr^{-1} while the minimal value toward the center of the ring is relatively close to 1.0×10^{-13} erg s^{-1} cm^{-2} sr^{-1}.

To further verify that the ring-like feature at the tip is not an image artifact, the moment 0 map was created for the WSRT and GMRT maps individually, which both show a dip toward the same location that is seen in the full combined map (see Figure 11). This gives further confidence that this drop in emission toward the center of the tip is a real feature. Additionally, Figure 11 also indicates that the weaker emission in the eastern part of the ring might be attributed to an artifact in the GMRT data cube.

Lastly, we also present the average spectrum with the best possible S/N extracted from inside the ring, see Figure 12. This spectrum shows a non-Gaussian skewed line profile, but because of the relatively high noise rms in the data it is not

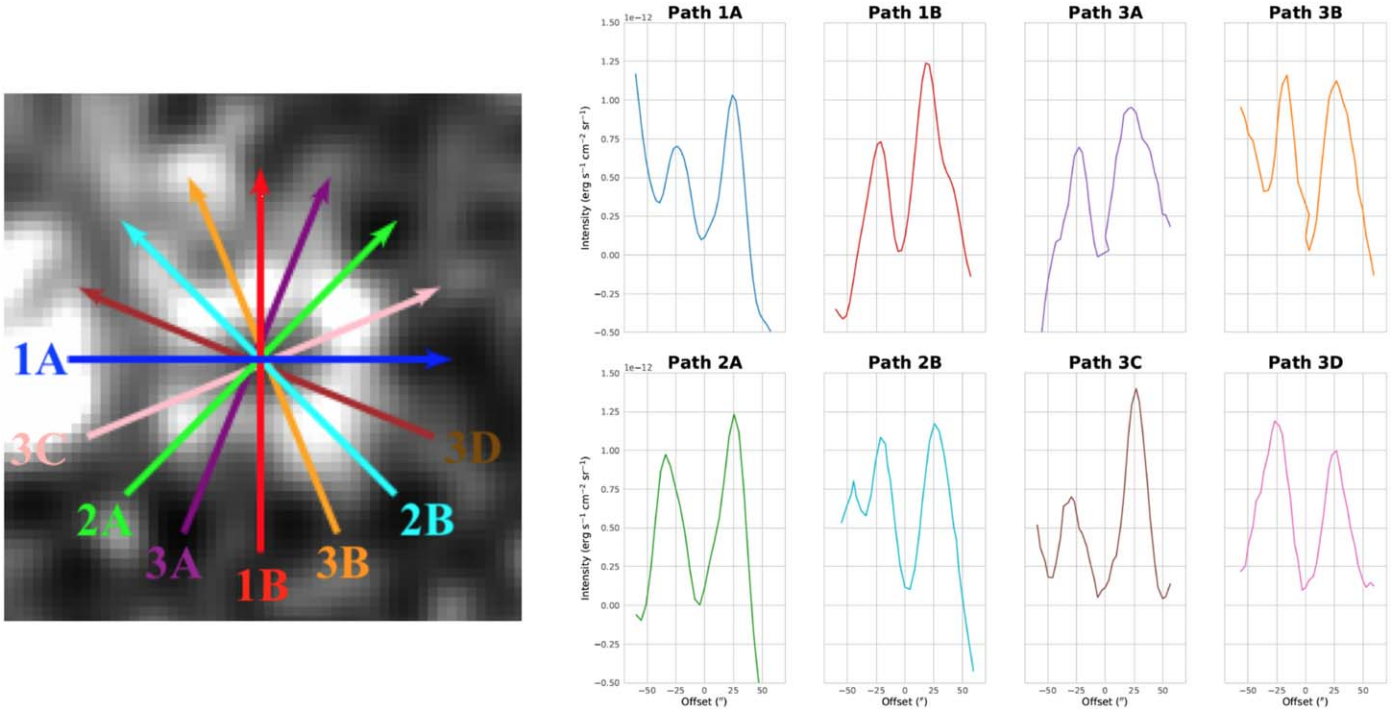

Figure 10. Left: the different paths that were defined over the H I ring-like feature on top of the H I integrated intensity map. Right: the H I emission profiles over the ring for the eight individual paths defined on the left.

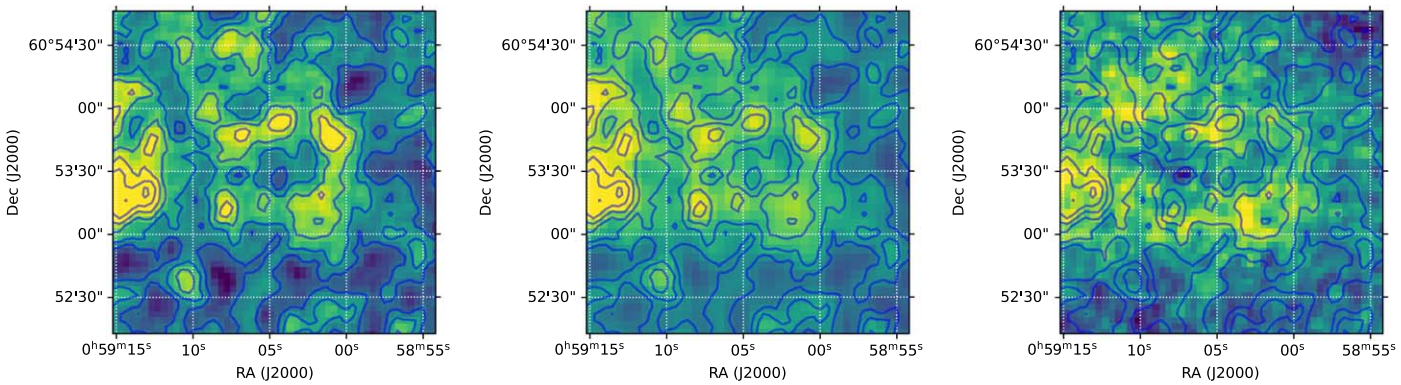

Figure 11. Left: the ring seen in the moment 0 map from the combined cube with contours from 0.1 to 0.225 Jy km s^{-1} in steps of 0.025 Jy km s^{-1}. Center: the same field in the moment 0 map from the WSRT data with the contours from the combined cube overlaid. Right: the same field in the moment 0 map from the GMRT data with the contours from the combined cube overlaid. These plots show that the ring is seen in both interferometric data sets and so is not an artifact from a single telescope that has propagated into our combined cube. They also reveal that there appears to be some substructure in the ring.

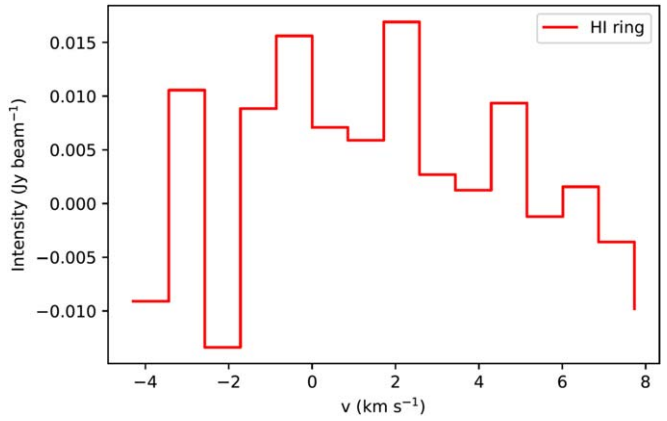

Figure 12. The average H I spectrum obtained from inside the ring at the tip of IC 63. As expected the noise is fairly high, making it challenging to conclude on the presence of self absorption.

possible to assess whether this non-Gaussian profile is due to self absorption or not.

ORCID iDs

Lars Bonne https://orcid.org/0000-0002-0915-4853
B-G Andersson https://orcid.org/0000-0001-6717-0686
Robert Minchin https://orcid.org/0000-0002-1261-6641
Archana Soam https://orcid.org/0000-0002-6386-2906
Kristin Kulas https://orcid.org/0000-0002-1868-4485
Janik Karoly https://orcid.org/0000-0001-5996-3600
Lewis B. G. Knee https://orcid.org/0000-0002-9342-9003
Siddharth Kumar https://orcid.org/0000-0002-5816-6623
Nirupam Roy https://orcid.org/0000-0001-9829-7727

References

Andersson, B.-G., Piirola, V., De Buizer, J., et al. 2013, ApJ, 775, 84
Andrews, H., Peeters, E., Tielens, A. G. G. M., & Okada, Y. 2018, A&A, 619, A170
Astropy Collaboration, Robitaille, T. P., Tollerud, E. J., et al. 2013, A&A, 558, A33
Bertoldi, F., & Draine, B. T. 1996, ApJ, 458, 222
Bisbas, T. G., Bell, T. A., Viti, S., Yates, J., & Barlow, M. J. 2012, MNRAS, 427, 2100
Blouin, D., McCutcheon, W. H., Dewdney, P. E., et al. 1997, MNRAS, 287, 455
Bonne, L., Schneider, N., Bontemps, S., et al. 2020, A&A, 641, A17
Bonne, L., Schneider, N., García, P., et al. 2022, ApJ, 935, 171
Condon, J. J., Cotton, W. D., Greisen, E. W., et al. 1998, AJ, 115, 1693
Draine, B. T. 1978, ApJS, 36, 595
Draine, B. T., & Bertoldi, F. 1996, ApJ, 468, 269
Fleming, B., France, K., Lupu, R. E., & McCandliss, S. R. 2010, ApJ, 725, 159
France, K., Andersson, B. G., McCandliss, S. R., & Feldman, P. D. 2005, ApJ, 628, 750
Gierens, K. M., Stutzki, J., & Winnewisser, G. 1992, A&A, 259, 271
Greisen, E. W. 2003, in AIPS, the VLA, and the VLBA, ed. A. Heck, Vol. 285 (Dordrecht: Kluwer), 109
Guan, X., Stutzki, J., Graf, U. U., et al. 2012, A&A, 542, L4
Güver, T., & Özel, F. 2009, MNRAS, 400, 2050
Heyminck, S., Graf, U. U., Güsten, R., et al. 2012, A&A, 542, L1
Hollenbach, D. J., & Tielens, A. G. G. M. 1999, RvMP, 71, 173
Jansen, D. J., van Dishoeck, E. F., & Black, J. H. 1994, A&A, 282, 605
Kabanovic, S., Schneider, N., Ossenkopf-Okada, V., et al. 2022, A&A, 659, A36
Karr, J. L., Noriega-Crespo, A., & Martin, P. G. 2005, AJ, 129, 954
Kaufman, M. J., Wolfire, M. G., Hollenbach, D. J., & Luhman, M. L. 1999, ApJ, 527, 795
Kurucz, R. L. 1979, ApJS, 40, 1
Landecker, T. L., Dewdney, P. E., Burgess, T. A., et al. 2000, A&AS, 145, 509
Le Petit, F., Nehmé, C., Le Bourlot, J., & Roueff, E. 2006, ApJS, 164, 506
Maillard, V., Bron, E., & Le Petit, F. 2021, A&A, 656, A65
McClure-Griffiths, N. M., Dickey, J. M., Gaensler, B. M., et al. 2005, ApJS, 158, 178
Pound, M. W., & Wolfire, M. G. 2008, in ASP Conf. Ser. 394, Astronomical Data Analysis Software and Systems XVII, ed. R. W. Argyle, P. S. Bunclark, & J. R. Lewis (San Francisco, CA: ASP), 654
Pound, M. W., & Wolfire, M. G. 2023, AJ, 165, 25
Risacher, C., Güsten, R., Stutzki, J., et al. 2016, A&A, 595, A34
Risacher, C., Güsten, R., Stutzki, J., et al. 2018, JAI, 7, 1840014
Röllig, M., Abel, N. P., Bell, T., et al. 2007, A&A, 467, 187
Roy, J., Gupta, Y., Pen, U.-L., et al. 2010, ExA, 28, 25
Sault, R. J., Teuben, P. J., & Wright, M. C. H. 1995, in ASP Conf. Ser. 77, Astronomical Data Analysis Software and Systems IV, ed. R. A. Shaw, H. E. Payne, & J. J. E. Hayes (San Francisco, CA: ASP), 433
Schmiedeke, A., Schilke, P., Möller, T., et al. 2016, A&A, 588, A143
Schneider, N., Simon, R., Guevara, C., et al. 2020, PASP, 132, 104301
Seifried, D., Beuther, H., Walch, S., et al. 2022, MNRAS, 512, 4765
Soam, A., Andersson, B. G., Karoly, J., DeWitt, C., & Richter, M. 2021a, ApJ, 923, 107
Soam, A., Andersson, B. G., Straižys, V., et al. 2021b, AJ, 161, 149
Soam, A., Maheswar, G., Lee, C. W., Neha, S., & Andersson, B. G. 2017, MNRAS, 465, 559
Sternberg, A., & Dalgarno, A. 1995, ApJS, 99, 565
Sternberg, A., Le Petit, F., Roueff, E., & Le Bourlot, J. 2014, ApJ, 790, 10
Stoerzer, H., Stutzki, J., & Sternberg, A. 1996, A&A, 310, 592
Störzer, H., & Hollenbach, D. 1998, ApJ, 495, 853
Sugitani, K., Fukui, Y., & Ogura, K. 1991, ApJS, 77, 59
Taylor, A. R., Gibson, S. J., Peracaula, M., et al. 2003, AJ, 125, 3145
Taylor, A. R., Leahy, D. A., Tian, W. W., et al. 2017, AJ, 153, 113

Tielens, A. G. G. M., & Hollenbach, D. 1985, ApJ, 291, 722
Tiwari, M., Karim, R., Pound, M. W., et al. 2021, ApJ, 914, 117
Van De Putte, D., Gordon, K. D., Roman-Duval, J., et al. 2020, ApJ, 888, 22
van Leeuwen, F. 2007, A&A, 474, 653
Wang, Y., Bihr, S., Beuther, H., et al. 2020, A&A, 634, A139
Wilson, T. L., Rohlfs, K., & Hüttemeister, S. 2009, Tools of Radio Astronomy (Berlin: Springer)
Witt, A. N., Stecher, T. P., Boroson, T. A., & Bohlin, R. C. 1989, ApJL, 336, L21
Wolfire, M. G., Vallini, L., & Chevance, M. 2022, ARA&A, 60, 247
Young, E. T., Becklin, E. E., Marcum, P. M., et al. 2012, ApJL, 749, L17